State-feedback control of an internal rotor for propelling and steering a flexible fish-inspired underwater vehicle

Jinseong Lee[1], Brian Free[2], Shyline Santana[3], Derek A. Paley[4]

***Abstract*— This paper addresses the swimming dynamics and control of a flexible fish-inspired robot based on closed-loop control of an internal reaction wheel. Previous studies have shown that the dynamics of a rigid swimming robot are analogous to the canonical Chaplygin sleigh, due to the nonholonomic constraint imposed by the Kutta condition applied to the fish-like tail. The Chaplygin-sleigh dynamics are used here to design a propulsion and steering controller for a flexible swimming robot using state feedback. The desired average heading angle is achieved using a torque calculated from the instantaneous heading angle and rate. This feedback law stabilizes a limit cycle about the desired heading angle and produces forward swimming motion. Analysis of a global bifurcation in the dynamics under feedback control reveals the set of control gains that yield the desired limit cycle. Simulations illustrate planar swimming motion and preliminary experimental results are provided.**

I. Introduction

Unmanned underwater vehicles have applications including maritime surveillance [1], inspection of underwater structure [2], and search and recovery missions [3]. Two of the challenges of existing underwater vehicles are achieving high maneuverability and long endurance. Motivated by the agile maneuvers of swimming fish evolved over millions of years, fish-inspired robots may be capable of agile maneuvers, energy efficiency, and stealthy swimming [4]–[6].

A fish-inspired robot made of soft material helps overcome some of the limitations of existing rigid designs. Many fish robots are comprised of two partitions, the main body and tail fin, and an exposed articulated joint may limit agility due to the interaction with water [7], [8]. There have been various attempts to improve the performance of the mechanisms of external actuators such as screws, fins, or wings of underwater vehicles [6], [9], [10]. However, these types of actuators have drawbacks in that they may generate excessive noise, vibration, corrosion, propulsive inefficiency, or even adverse environmental side effects [11].

Internal actuation commonly used for spacecraft or satellites [12] is an alternative approach to improve maneuverability by rotating a reaction wheel. The spinning rotor follows a periodic profile to rotate the body by the conservation of angular momentum, and the rotating body generates thrust for propulsion by interaction with the surrounding fluid. Internal motors contained in a pressure vessel are prevented from contacting the water, reducing motor corrosion and vibration.

Previous works demonstrated translational motion of a swimming robot using internal actuation such as a spinning rotor or mass displacement [13]–[15]. Several authors described the swimming motion of Chaplygin sleigh using an internal rotor [16], [17] and heading-angle tracking using attitude feedback [15], [17].

The swimming motion of a rigid fish robot is known to have a nonholonomic constraint at the trailing edge due to the Kutta condition [18], analogous to the Chaplygin sleigh [19]. The trailing edge of the sleigh is subject to a nonholonomic constraint that permits no velocity in the perpendicular direction. A rotating reaction wheel at the center of mass generates the sleigh's translational motion, like the forward swimming motion of a fish robot [15], [19].

To steer a swimming robot using a reaction wheel, various torque profiles such as symmetric, asymmetric, and impulsive have been used [13], [19]. Other works focus on the analysis of the energy of the Chaplygin sleigh's motion as a piecewise-smooth nonholonomic constraint and simulate transitions between distinct dynamics belonging to the slip and stick modes [15], [20]. However, these prior works are limited to solid-bodied robots [15], [17]–[20], and do not use a state-feedback control.

Prior work within our research group has studied the control of novel underwater vehicles. Closed-loop control of a torque-driven flexible fish robot for flow-relative swimming motion was accomplished in a flow tank using pressure sensor data for estimation [11]. Artificial lateral lines comprised of pressure sensors were also used to estimate the location of vortices and actuate a rigid fish robot through a vortex street in a Kármán gaiting pattern [21]. This paper is an extension of these works to develop free-swimming capabilities with an internal rotor.

Here, we present swimming and steering of a novel bioinspired underwater vehicle using a reaction wheel as an internal actuator. The contributions of this paper are (1) the fish-inspired design of a free-swimming underwater vehicle

This work is supported by the Office of Naval Research under Grant No. N000141512246. Brian Free is supported by the National Science Foundation Graduate Research Fellowship Program under Grant No. DGE 1322106. S. Santana was suppported by NSF TREND REU program of the University of Maryland under Grant No. 175679

[1]Jinseong Lee is a graduate research assistant in the Department of Aerospace Engineering at the University of Maryland, College Park, MD, 20742, USA. jlee1266@umd.edu

[2]Brian Free is a graduate research assistant in the Department of Aerospace Engineering at the University of Maryland, College Park, MD, 20742, USA. bfree@umd.edu

[3]Shyline Santana is an undergraduate student in the Department of Physics at the University of Puerto Rico, Rio Piedras Campus, San Juan, Puerto Rico, 00931. shyline.santana@upr.edu

[4]Derek A. Paley is the Willis H. Young Jr. Professor of Aerospace Engineering Education in the Department of Aerospace Engineering and the Institute for Systems Research, University of Maryland, College Park, MD 20742, USA dpaley@umd.edu

made of flexible silicone and 3D-printed material; (2) state-feedback control for heading control using reaction-wheel torque including preliminary experimental demonstration of the closed-loop results; and (3) limit cycle and bifurcation analysis of the closed-loop dynamics.

The outline of this paper is as follows. Section II provides mathematical background on the Chaplygin sleigh dynamics and motor equations. Section III presents the feedback control law and analyzes the closed-loop system to determine the range of control gains that produce the desired motion. Section IV presents the design of an internally actuated robot and preliminary experimental results. Section V summarizes the paper and discusses ongoing work.

II. Background

This section describes the mathematical modeling for swimming motion under a nonholonomic constraint using the Chaplygin sleigh dynamics and discusses the motor dynamics for internal actuation of the fish robot.

A. Chaplygin sleigh dynamics

Let x and y be the center of mass of the Chaplygin sleigh, l be the distance from the center of mass to a fixed knife edge. θ represents the heading angle in the inertial coordinates, as shown in Fig. 1. The rotation angle of the reaction wheel with respect to the body frame is ψ. The total mass of the body and wheel is denoted as m. The moment of inertia of the body about the z-axis is J and that of the reaction wheel is J_w. Consider a body-fixed reference frame X_b and Y_b. The translational velocity of the robot has magnitude v and is constrained to point in the X_b direction. This nonholonomic constraint is expressed as [16]

$$\dot{x}\sin\theta - \dot{y}\cos\theta + l\dot{\theta} = 0. \tag{1}$$

The velocity of the center of mass of the body is described in terms of the velocities $\dot{x}_w$ and $\dot{y}_w$ of the wheel

$$\begin{aligned} \dot{x} &= \dot{x}_w - l\dot{\theta}\sin\theta \\ \dot{y} &= \dot{y}_w + l\dot{\theta}\cos\theta, \end{aligned} \tag{2}$$

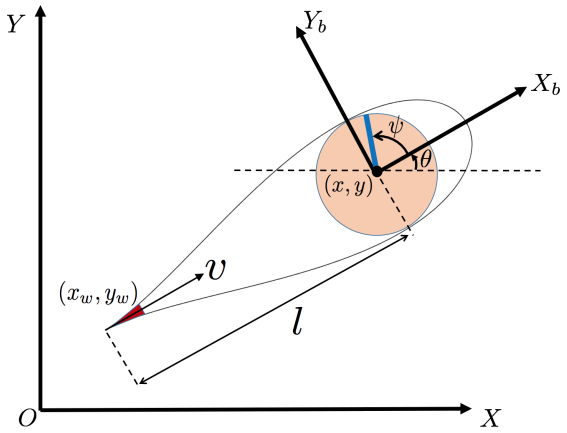

Fig. 1: Coordinates for a fish robot modelled as a Chaplygin sleigh

where $\dot{x}_\omega$ and $\dot{y}_w$ are equivalent to $v\cos\theta$ and $v\sin\theta$, respectively. When an input torque is applied to the body, the drag-free equations of motion are [16], [22]

$$\dot{x} = v\cos\theta - l\dot{\theta}\sin\theta \tag{3}$$

$$\dot{y} = v\sin\theta + l\dot{\theta}\cos\theta \tag{4}$$

$$\dot{v} = l\dot{\theta}^2 \tag{5}$$

$$\ddot{\theta} = -\frac{mlv\dot{\theta} + u}{J + ml^2} \tag{6}$$

$$\ddot{\psi} = \frac{J_w mlv\dot{\theta} + (J + J_w + ml^2)u}{(J + ml^2)J_w} \tag{7}$$

where $\dot{\psi}$ is the angular rate of the wheel. Applying input torque u to the wheel in (6) enables the robot to swim and steer.

B. Motor model

To generate input torque using a DC motor and a wheel, we introduce the following relationships:

$$\tau_m = K_\tau i, \qquad e = K_e\Omega, \tag{8}$$

where K_τ is the motor torque constant, τ_m is motor torque, i is current, K_e is the back EMF (Electromotive Force) constant, Ω is the motor angular rate, and e is the back-EMF voltage. Modeling the motor system as a closed-loop RLC circuit yields $V = L\frac{di}{dt} + iR + e$. Neglecting the inductance L,

$$V = iR + K_e\Omega, \tag{9}$$

where V denotes applied total voltage and R is the resistance of the motor winding. When a torque τ_m is applied by the motor, it is amplified by the gear ratio K_g, thus the input torque applied to the reaction wheel is $u = K_g\tau_m$. The angular rate $\dot{\psi}$ of the reaction wheel, which is measured by an encoder, is reduced by the gear ratio to $\dot{\psi} = \Omega/K_g$. Substituting (8) and the gear ratio into (9) yields the relationships

$$V = \frac{\tau_m}{K_\tau}R + K_eK_g\dot{\psi} \tag{10}$$

$$= \frac{u}{K_gK_\tau}R + K_eK_g\dot{\psi}, \tag{11}$$

$$u = C_1V - C_2\dot{\psi}, \tag{12}$$

where the constants are $C_1 = K_\tau K_g/R$ and $C_2 = K_\tau K_e K_g^2/R$.

Since voltage V applied to the motor is proportional to the duty ratio of Pulse Width Modulation (PWM), then $V = V_{\max}\mathrm{PWM}/255$ and any arbitrary torque profile can be determined by PWM. The relation between wheel torque and PWM is

$$u = \frac{K_\tau K_g}{R}\left(V_{\max}\frac{\mathrm{PWM}}{255} - K_eK_g\dot{\psi}\right). \tag{13}$$

The PWM corresponding to u is

$$\mathrm{PWM} = \frac{255R}{K_\tau K_g V_{\max}}\left(u + \frac{K_\tau K_e K_g^2\dot{\psi}}{R}\right). \tag{14}$$

To characterize the motor used in experiments, K_τ and K_e were determined offline as follows. Stall current was measured at 3 A when a torque load of 0.595 Nm was applied

Parameter	Value	Units	Parameter	Value	Units
K_τ	0.01	Nm/A	Saturation	255	-
K_e	0.01	Nms	Deadband	26	-
K_g	20.4	-	R	4	ohm
m	1.8	kg	$K1$	1	-
l	0.2	m	$K2$	4	-
b	0.045	kgm^2	d	0.5	sec^{-1}

TABLE I: Parameters for motor (top) and simulation (bottom)

to the motor. A maximum speed of 500 rpm with free load was measured at a rated voltage (12V). Then, K_τ and K_e in (8) were determined to be 0.01 [Nm/A] and 0.01 [Vs], respectively. Given the resistance R and a gear ratio of K_g 20.4, plugging them into (11) yields C_1 = 0.05 [Nm/V] and C_2= 0.01 [Nms] in (12).

The PWM range is from 0 to 255 and increasing PWM generates more torque by applying more voltage. However, the motor eventually reaches saturation in generating torque. Hence, if an input torque requires more than the physical upper limit of motor torque, its PWM command stays at 255, while maintaining the maximum torque level. In addition, there also exists a deadband where small PWM commands under lower limit do not generate any torque.

III. State-feedback control design and analysis

This section presents the design of a state-feedback control for the dynamic model based on the Chaplygin sleigh. The control law causes a bifurcation of the closed-loop system that yields either desired or undesired limit-cycle behavior, depending on the control gains.

A. State-feedback control design

For closed-loop control of heading angle, control input torque u to the wheel in (6) uses feedback of angular rate $\dot{\theta}$=ω and orientation θ. Let θ_d be the desired heading angle. Consider the control law

$$u = b\left(-K_1\omega - K_2\sin(\theta_d - \theta)\right), \tag{15}$$

where b is the moment of inertia $J+ml^2$, K_1 and K_2 are the feedback gains, and the PWM input is determined by using (15) in (14).

In state-space form, ignoring the (x,y) position and wheel angle ψ and rate $\dot{\psi}$, the reduced state vector, z is $\begin{bmatrix} v & \theta & \omega \end{bmatrix}^T$. The feedback law (15) with drag coefficient $d \geq 0$, mass $m > 0$, length $l > 0$, moment of inertia $b > 0$, $K_1 > 0$, and $K_2 > 0$ results in the closed-loop dynamics:

$$\dot{v} = l\omega^2 - dv \tag{16}$$

$$\dot{\theta} = \omega \tag{17}$$

$$\dot{\omega} = -\frac{ml}{b}v\omega + K_1\omega + K_2\sin(\theta_d - \theta), \tag{18}$$

Evaluating (18) with θ_d=θ and $\dot{\omega}$=0 predicts the average swimming speed to be $\bar{v} = \frac{K_1 b}{ml}$.

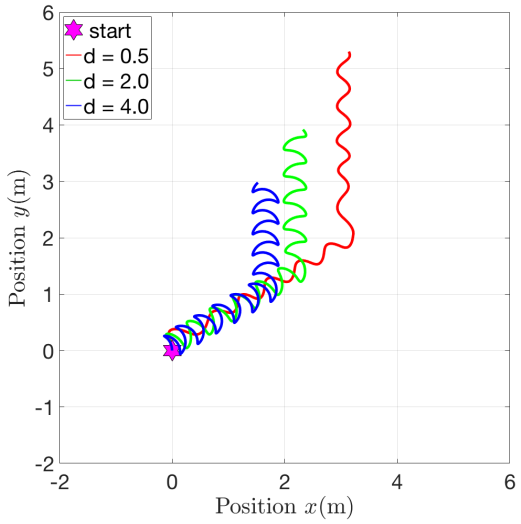

Fig. 2: Simulation with varying drag coefficient. Desired heading angle θ_d is set to 30° until 20 seconds and then becomes 90°

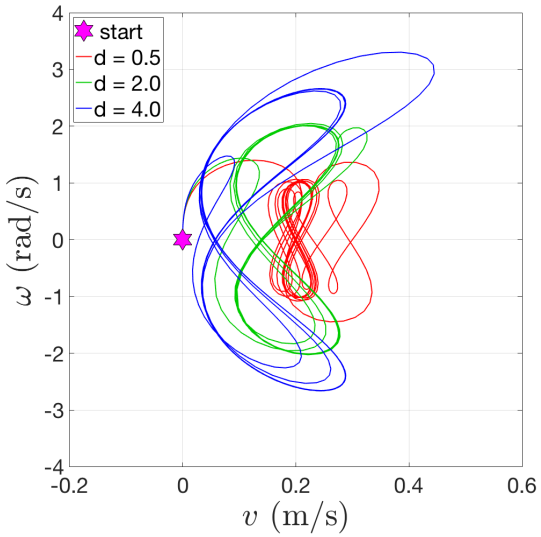

Fig. 3: Simulated swimming speed vs. angular rate for various drag coefficients

Simulations using the parameters in Table I are shown in Fig. 2 and 3. Changing the reference heading angle θ_d during swimming steers the vehicle to the new heading reference. The forward swimming distance decreases when the drag coefficient increases and the heading angle exhibits larger oscillations as shown in Fig. 2. The relationship between swimming speed and angular rate under drag creates a limit cycle as shown in Fig. 3. As the drag coefficient increases, the limit cycle shifts to the left and the amplitude of ω increases.

B. Bifurcation analysis of closed-loop system

The closed-loop system exhibits bifurcation behavior in which the desired limit cycle corresponding to forward swimming behavior is achieved only for certain values of the

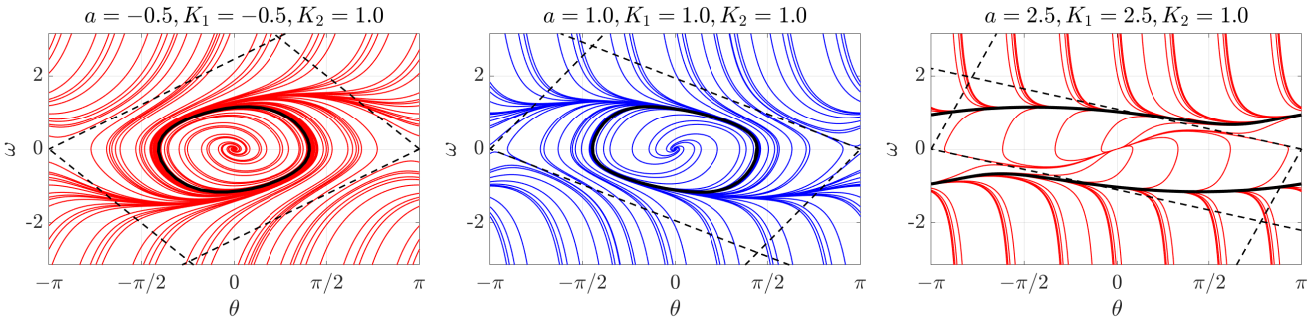

Fig. 4: Bifurcations of the nonlinear pendulum in phase space: (Left) unstable limit cycle for $-2\sqrt{K_2} < a < 0$; (Middle) stable limit cycle for $0 < a < 2\sqrt{K_2}$; and (Right) two stable limit cycles for $a > a^* > 2\sqrt{K_2}$. Black dashed lines are the stable and unstable manifolds of the linearization of the saddle point at $\theta = \pm\pi$.

control gains K_1 and K_2. For other values of these gains, the angular velocity in the resulting limit cycle does not switch signs and the model fish spins in a circle. We now establish the existence of the desired limit cycle and determine the allowable range of gains.

First, (16) can be re-written as

$$\dot{v} = d\left(\frac{l}{d}\omega^2 - v\right) \tag{19}$$

For $\dot{\omega} = 0$, i.e., $\omega = \omega_0$ constant, the subsystem in (19) exponential stabilizes $v = \frac{l}{d}\omega_0^2$ with Lyapunov function

$$V_1(v) = \frac{1}{2}\left(\frac{l}{d}\omega_0^2 - v\right)^2.$$

For $d \gg 1$, there is a time-scale separation between the v subsystem (fast) and the (θ, ω) subsystem (slow). Let $a = \frac{ml^2}{bd} > 0$. Without loss of generality, let reference angle $\theta_d = 0$. Substituting the solution $v = \frac{l}{d}\omega^2$ (with ω treated as a constant) into the slow subsystem (17)–(18) yields

$$\begin{aligned} \dot{\theta} &= \omega \\ \dot{\omega} &= -a\omega^3 + K_1\omega - K_2\sin\theta, \end{aligned} \tag{20}$$

which is the equation of motion of a pendulum with nonlinear damping and natural frequency $\sqrt{K_2}$. The system (20) has equilibrium points $(0,0)$ and $(\pm\pi, 0)$. As we will show, it also has a limit cycle for certain values of a and K_1.

The Jacobian of (20) is

$$\frac{\partial f}{\partial z} = \begin{bmatrix} 0 & 1 \\ -K_2\cos\theta & -3a\omega^2 + K_1 \end{bmatrix},$$

which implies the origin $(0,0)$ is an unstable node or focus and the point $(\pm\pi, 0)$ is a saddle. To facilitate analysis of the limit cycle in (20), let $K_1 = a$, which yields

$$\dot{\theta} = \omega \tag{21}$$

$$\dot{\omega} = a(-\omega^3 + \omega) - K_2\sin\theta. \tag{22}$$

The linearization of (21)–(22) at $(\theta, \omega) = (0,0)$ becomes

$$\left.\frac{\partial f}{\partial z}\right|_{(0,0)} = \begin{bmatrix} 0 & 1 \\ -K_2 & a \end{bmatrix},$$

which has eigenvalues $\lambda_{1,2} = \frac{a}{2} \pm \frac{1}{2}\sqrt{a^2 - 4K_2}$. Therefore, the eigenvalues are complex if $|a| < 2\sqrt{K_2}$. Consider a as a bifurcation parameter. For $-2\sqrt{K_2} < a < 0$, the origin is a stable focus and, for $0 < a < 2\sqrt{K_2}$, the origin is an unstable focus. Therefore, as a passes through zero, there is a Hopf bifurcation [23] giving rise to a stable limit cycle for $0 < a < 2\sqrt{K_2}$ (and an unstable limit cycle for $-2\sqrt{K_2} < a < 0$).

For some $a^* > 0$, there is another global bifurcation and the limit cycle splits into two limit cycles that orbit the phase cylinder [24]: one in the positive direction and one in the negative direction. This global bifurcation occurs when the limit cycle tangentially intersects the stable manifold of the saddle point at $\theta = \pm\pi$.

For the case where $K_1 \neq a$, a numerical analysis to determine the presence of the desired limit cycle uses the following scheme. For a given set of parameters $a, K_1, K_2 > 0$, choose an initial condition near the origin $(\theta, \omega) = (0,0)$, which is an unstable fixed point. Simulate the system dynamics for a length of time observed to be much higher than the period of the limit cycle. If, at the end of the simulation, $|\theta| > \pi$, then the desirable limit cycle is not present. This bifurcation analysis shows that if a trajectory reaches the saddle point $(\pm\pi, 0)$, the desired limit cycle breaks into two undesired ones as shown in Fig. 4.

To determine which gains (K_1, K_2) result in the desired behavior for a given set of physical parameters a, we

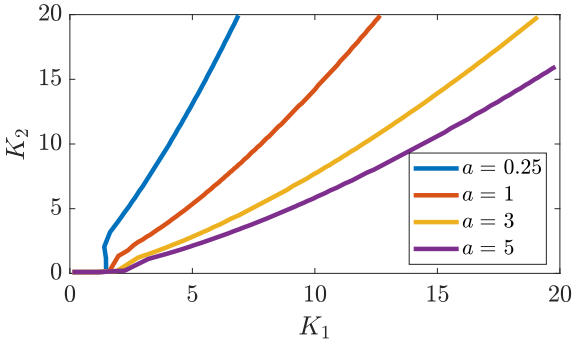

Fig. 5: Numerical bifurcation analysis: the region above a given curve results in the desired limit cycle.

performed this numurical simulation scheme across many values of K_1, K_2, and a. Fig. 5 shows the results where, for a given a, pairs (K_1, K_2) above the curve result in the desirable limit cycle and those below do not. Gain K_1 has an indirect effect on the amplitude of oscillations about the desired heading angle: larger K_1 creates larger heading oscillations and faster average speed v. Gain K_2 appears in the dynamics as the square of the natural frequency of a pendulum system, so oscillations about the desired heading angle occur at frequency $\sqrt{K_2}$. This analysis shows that for a given K_2, K_1 can be increased only up to the bounding curve in Fig. 5.

IV. EXPERIMENTAL TESTBED AND RESULTS

We designed a fish robot made of flexible silicon rubber and 3D-printed material as shown in Fig. 6. Inspired by the body shape of carangiform fish [25], the robot was modeled with a Bluegill side silhouette and a Joukowski airfoil top silhouette, to be used in the mathematical analysis of flow sensing [21].

The robot body is made of Dragon Skin 10, a flexible silicon rubber that is easily molded to any shape. Its flexibility provides tail flapping motion when the reaction wheel rotates. To accommodate the motor and electronic components, the robot contains a pressure vessel made of 3D-printed PLA plastic coated with epoxy to be watertight. To stabilize and restore the body against rolling motion, the reaction wheel is placed just below the center of buoyancy so that the center of mass is lower than the center of buoyancy. The physical specification is provided in Table II.

The robot is embedded with various hardware components shown in Fig. 7. It includes the ARM Cortex-M4 micro processor, reaction wheel, Pololu 20.4:1 geared DC motor, motor driver, 48 pulse rotary encoder, 11.1V LiPo battery, micro SD card, custom interface PCB, power switch, umbilical port for charging and programming, color LEDs, 5/3.3 V regulators, multiplexer, 2.4GHz XBee transceiver, and MPU9250 IMU sensor. The communication between the micro processor and the devices is via serial SPI and I2C, and onboard data is stored in a micro SD card for data analysis. A XBee module transmits data wireless to a remote PC in real time. Wireless communication supports several commands such as start and stop for swimming, heading angle reset, feedback gain setting, and retrieving the files saved on the SD card. The RGB LEDs are activated to convey the state of the robot while swimming.

Item	Robot	Wheel	Units
Size	317(L) x 80(W) x 150(H)	59(D)	mm
Mass	1.4	0.4	kg
Inertia	0.005	0.0003	kgm^2

TABLE II: Fish robot specification

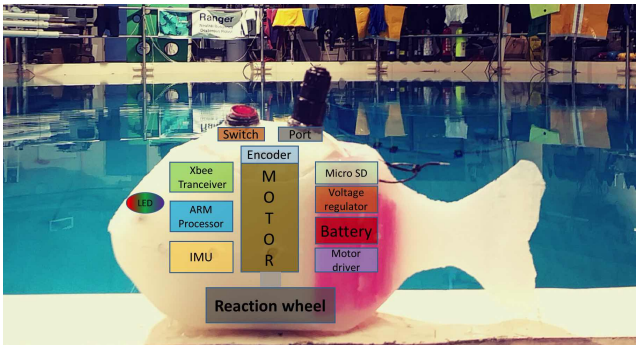

Fig. 6: A reaction-wheel-based swimming robot made from flexible material. All electronic modules are contained in a watertight pressure vessel

Swimming motion and steering tests for a submerged vehicle have been demonstrated in the Neutral Buoyancy Research Facility of the University of Maryland (Fig. 8b). The facility is equipped with 16 Qualisys underwater cameras to track two reflective markers mounted on either side of the fish robot. The desired heading angle is set to zero when the reaction wheel starts to spin and the robot swims forward. To verify the trajectory and heading angle, the trajectory from the Qualisys camera system is depicted in Fig. 8a. The heading angle error may be caused by yaw rate drift of the IMU sensor, unmodeled motor friction, or water currents around the bottom of the water tank (Fig. 8b).

V. CONCLUSION

This paper presents a novel design of a flexible swimming robot actuated by an internal reaction wheel for closed-loop control of heading control. We examine a dynamic model based on the Chaplygin sleigh. A state-feedback control law propels the robot along the desired heading angle. Bifurcation analysis shows that the swimming motion of a fish robot is affected by the stability of a limit cycle in phase space. We determine the set of gains for which swimming motion occurs. Simulations illustrate tracking a heading reference and preliminary underwater tests demonstrate successful swimming motion. In ongoing work, we seek to refine the model to include rotational drag from the fluid and friction in the motor dynamics. Furthermore, we seek to implement flow sensing and multi-vehicle control.

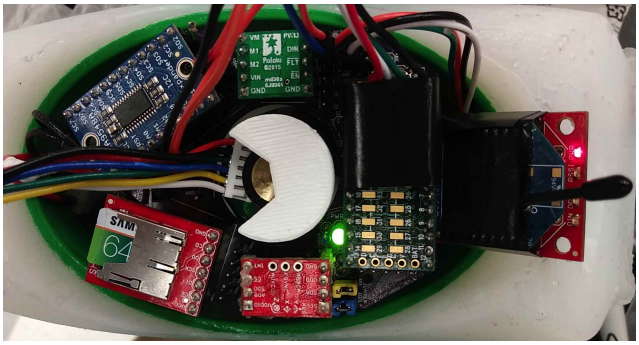

Fig. 7: A custom PCB interfaces electronic devices in a 3D-printed pressure vessel. The two-layer PCB is designed to have an elliptical shape to fit the container

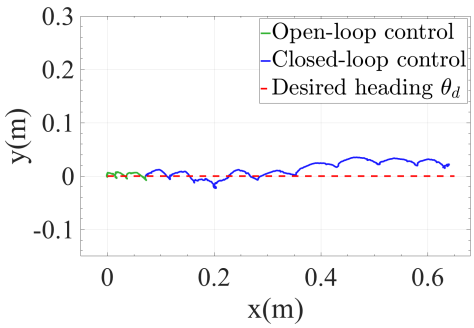

(a)

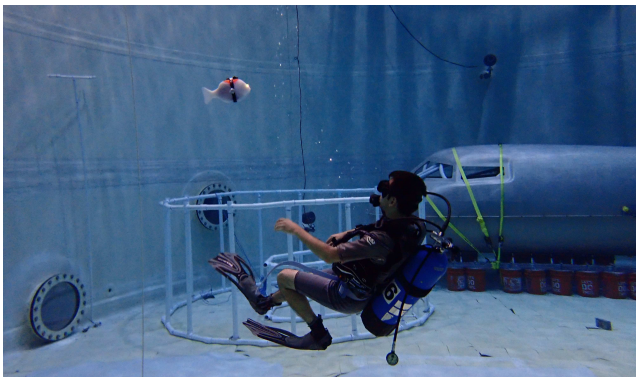

(b)

Fig. 8: (a) Trajectory captured by the Qualisys motion capture system in (b) the UMD Neutral Buoyancy Research Facility

ACKNOWLEDGMENT

This work is based upon work supported by the Office of Naval Research under Grant No. N000141612208. The authors thank Chris Arreza, Travis Burch, Jeremy Chang, Tin Nguyen, Mukund Patnaik, Jenny Mei, Brynne Schonne, and Artur Wolek for their support and valuable advice.

REFERENCES

[1] A. Maguer, R. Dymond, A. Grati, R. Stoner, P. Guerrini, L. Troiano, and A. Alvarez, "Ocean gliders payloads for persistent maritime surveillance and monitoring," in *Oceans-San Diego*, 2013, pp. 1–8.

[2] P. Ozog, N. Carlevaris-Bianco, A. Kim, and R. M. Eustice, "Long-term mapping techniques for ship hull inspection and surveillance using an autonomous underwater vehicle," *Journal of Field Robotics*, vol. 33, no. 3, pp. 265–289, 2016.

[3] M. Purcell, D. Gallo, G. Packard, M. Dennett, M. Rothenbeck, A. Sherrell, and S. Pascaud, "Use of REMUS 6000 AUVs in the search for the Air France flight 447," in *OCEANS*, 2011, pp. 1–7.

[4] D. Rus and M. T. Tolley, "Design, fabrication and control of soft robots," *Nature*, vol. 521, no. 7553, p. 467, 2015.

[5] C. Zhou and K. Low, "Design and locomotion control of a biomimetic underwater vehicle with fin propulsion," *IEEE/ASME Transactions on Mechatronics*, vol. 17, no. 1, pp. 25–35, 2012.

[6] V. Kopman, J. Laut, F. Acquaviva, A. Rizzo, and M. Porfiri, "Dynamic modeling of a robotic fish propelled by a compliant tail," *IEEE Journal of Oceanic Engineering*, vol. 40, no. 1, pp. 209–221, 2015.

[7] J. L. Tangorra, S. N. Davidson, I. W. Hunter, P. G. Madden, G. V. Lauder, H. Dong, M. Bozkurttas, and R. Mittal, "The development of a biologically inspired propulsor for unmanned underwater vehicles," *IEEE Journal of Oceanic Engineering*, vol. 32, no. 3, pp. 533–550, 2007.

[8] B. P. Epps, P. V. y Alvarado, K. Youcef-Toumi, and A. H. Techet, "Swimming performance of a biomimetic compliant fish-like robot," *Experiments in fluids*, vol. 47, no. 6, p. 927, 2009.

[9] A. Borisov and I. Mamayev, "The dynamics of a Chaplygin sleigh," *Journal of Applied Mathematics and Mechanics*, vol. 73, no. 2, pp. 156–161, 2009.

[10] Z. Chen, J. Yu, A. Zhang, and F. Zhang, "Design and analysis of folding propulsion mechanism for hybrid-driven underwater gliders," *Ocean Engineering*, vol. 119, pp. 125–134, 2016.

[11] F. Zhang, P. Washington, and D. A. Paley, "A flexible, reaction-wheel-driven fish robot: Flow sensing and flow-relative control," in *American Control Conference*, 2016, pp. 1221–1226.

[12] P. Tsiotras, H. Shen, and C. Hall, "Satellite attitude control and power tracking with energy/momentum wheels," *Journal of Guidance, Control, and Dynamics*, vol. 24, no. 1, pp. 23–34, 2001.

[13] G. Refael and A. Degani, "A single-actuated swimming robot: Design, modelling, and experiments," *Journal of Intelligent & Robotic Systems*, 2018. [Online]. Available: https://doi.org/10.1007/s10846-018-0776-x

[14] I. A. Bizyaev, A. V. Borisov, and S. P. Kuznetsov, "Chaplygin sleigh with periodically oscillating internal mass," *Europhysics Letters*, vol. 119, no. 6, p. 60008, 2017.

[15] M. J. Fairchild, P. M. Hassing, S. D. Kelly, P. Pujari, and P. Tallapragada, "Single-input planar navigation via proportional heading control exploiting nonholonomic mechanics or vortex shedding," in *ASME Dynamic Systems and Control Conference and Bath/ASME Symposium on Fluid Power and Motion Control*, 2011, pp. 345–352.

[16] J. M. Osborne and D. V. Zenkov, "Steering the Chaplygin sleigh by a moving mass," in *Joint IEEE Conference on Decision and Control and European Control Conference*, 2005, pp. 1114–1118.

[17] S. D. Kelly, M. J. Fairchild, P. M. Hassing, and P. Tallapragada, "Proportional heading control for planar navigation: The Chaplygin beanie and fishlike robotic swimming," in *American Control Conference*, 2012, pp. 4885–4890.

[18] P. Tallapragada and S. D. Kelly, "Self-propulsion of free solid bodies with internal rotors via localized singular vortex shedding in planar ideal fluids," *The European Physical Journal Special Topics*, vol. 224, no. 17-18, pp. 3185–3197, 2015.

[19] P. Tallapragada and V. Fedonyuk, "Steering a Chaplygin sleigh using periodic impulses," *Journal of Computational and Nonlinear Dynamics*, vol. 12, no. 5, p. 054501, 2017.

[20] V. Fedonyuk and P. Tallapragada, "Stick–slip motion of the Chaplygin sleigh with a piecewise-smooth nonholonomic constraint," *Journal of Computational and Nonlinear Dynamics*, vol. 12, no. 3, p. 031021, 2017.

[21] B. Free, M. K. Patnaik, and D. A. Paley, "Observability-based path-planning and flow-relative control of a bioinspired sensor array in a Karman vortex street," in *American Control Conference*, 2017, pp. 548–554.

[22] J. T. L. Tuttle, "Studies of systems with nonholonomic constraints: The segway and the Chaplygin sleigh," Master's thesis, Purdue University, 2014.

[23] S. H. Strogatz, *Nonlinear dynamics and chaos with applications to physics, biology, chemistry, and engineering*. CRC Press, 2018.

[24] J. Guckenheimer and P. Holmes, *Nonlinear oscillations, dynamical systems, and bifurcations of vector fields*. Springer-Verlag New York, 1983, vol. 42.

[25] R. Salazar, G. Taylor, M. Khalid, and A. Abdelkefi, "Optimal design and energy harvesting performance of carangiform fish-like robotic system," *Smart Materials and Structures*, vol. 27, no. 7, p. 075045, 2018.